Earth's Future

RESEARCH ARTICLE
10.1029/2024EF004545

Projections of Peak Water Timing From the East Rongbuk Glacier, Mt. Everest, Using a Higher-Order Ice Flow Model

Tong Zhang[1,2], Yuzhe Wang[3], Wei Leng[4], Hongyu Zhao[1], Willliam Colgan[5], Che Wang[6], Minghu Ding[7], Weijun Sun[3], Wei Yang[2], Xin Li[2], Jiawen Ren[8], and Cunde Xiao[1]

[1]State Key Laboratory of Earth Surface Processes and Resource Ecology, Beijing Normal University, Beijing, China, [2]State Key Laboratory of Tibetan Plateau Earth System, Environment and Resources (TPESER), Institute of Tibetan Plateau Research, Chinese Academy of Sciences, Beijing, China, [3]College of Geography and Environment, Shandong Normal University, Jinan, China, [4]State Key Laboratory of Scientific and Engineering Computing, Beijing, China, [5]Geological Survey of Denmark and Greenland, Copenhagen, Denmark, [6]College of Resources, Environment and Tourism, Capital Normal University, Beijing, China, [7]Chinese Academy of Meteorological Sciences, Beijing, China, [8]Northwest Institute of Eco-Environment and Resources, Chinese Academy of Sciences, Lanzhou, China

Key Points:

- We conduct diagnostic and prognostic simulations of East Rongbuk Glacier, Mt. Everest
- The use of Robin inversion method during initialization suggests the presence of temperate basal ice
- We find East Rongbuk Glacier will likely reach maximum meltwater runoff around the middle of this century

Correspondence to:
W. Leng and C. Xiao,
wleng@lsec.cc.ac.cn;
cdxiao@bnu.edu.cn

Citation:
Zhang, T., Wang, Y., Leng, W., Zhao, H., Colgan, W., Wang, C., et al. (2024). Projections of peak water timing from the East Rongbuk Glacier, Mt. Everest, using a higher-order ice flow model. *Earth's Future*, *12*, e2024EF004545. https://doi.org/10.1029/2024EF004545

Received 14 JULY 2023
Accepted 3 APR 2024

Abstract In this study, we apply a three-dimensional (3D) thermomechanically coupled higher-order ice flow model to simulate the East Rongbuk Glacier (ERG), Mt. Everest. We first diagnostically investigate its present-day ice dynamic features in 2009 and then prognostically simulate the glacier during the time period 2010–2100. The ice flow model is initialized based on a Robin-type inversion method by conducting six sensitivity experiments relating to glacier thermal boundary conditions. We apply two different surface mass balance parameterizations in the model, and both of them can reproduce the observed ice volume loss (around 0.1 km^3) during 2010–2020. We find that ERG is likely to experience maximum meltwater runoff at the year 2030 under the SSP-126 scenario, while under SSP-370 and -585 scenarios, the peak water will both likely occur at around 2060. The ice dynamics may contribute more to ice loss as climate warms in time.

Plain Language Summary The melt of glaciers in High Mountain Asia (HMA) has great impacts on regional water resources and socioeconomy. But it is not an easy task to accurately predict their future changes. The East Rongbuk Glacier (ERG), Mt. Everest, is one of few glaciers in HMA that has relatively rich in situ data for conducting three-dimensional numerical projections. In this study, we first carefully invert basal frictions at the ice-bed interface according to observed ice surface velocities as a model initialization. Then, we drive the model and simulate the changes of ERG from 2010 to 2100. We validate our model by comparing our simulation results to observed ice volume loss during 2010–2020. We find that ERG will reach its maximum meltwater runoff at around 2030 and 2060 for the lower (SSP-126) and higher (SSP-585) emission scenarios, respectively.

1. Introduction

The glaciers of High Mountain Asia (HMA) are described as "water towers" that supply fresh water resources for over 1 billion people (Barnett et al., 2005; Immerzeel et al., 2010). To date, a number of remote sensing and simplified, large-scale model attempts have been made to assess the present-day and future glacier resources in HMA (Bhattacharya et al., 2021; Rounce et al., 2020). However, a plausible prediction of the future imbalance of these water towers remains highly uncertain, partly due to the lack of reliable modeling efforts (Hock et al., 2019; Rounce et al., 2020; Yao et al., 2022). Thus, there is a great urgency to more accurately assess the future changes of HMA glaciers.

Several obstacles exist preventing us from accurately understanding the general glacier evolution. First, due to the difficulties of obtaining in situ glaciological data (e.g., ice thickness), the majority of glacier geometries are estimated by model approaches (Farinotti et al., 2019; Millan et al., 2022). Second, the current large-scale glacier evolution models include very simple ice dynamic processes (Rounce et al., 2020). This leaves the future estimation of HMA ice volume changes still questionable. Finally, despite a growing number of satellite observations of HMA glaciers (e.g., ice surface velocity and elevation changes), our knowledge of englacial and subglacial thermodynamic characteristics of HMA glaciers remains poor (Azam et al., 2021; Gilbert et al., 2018, 2020; Liu et al., 2009; Miles et al., 2018), which seriously restricts the calibration of ice flow model parameters.

10.1029/2024EF004545

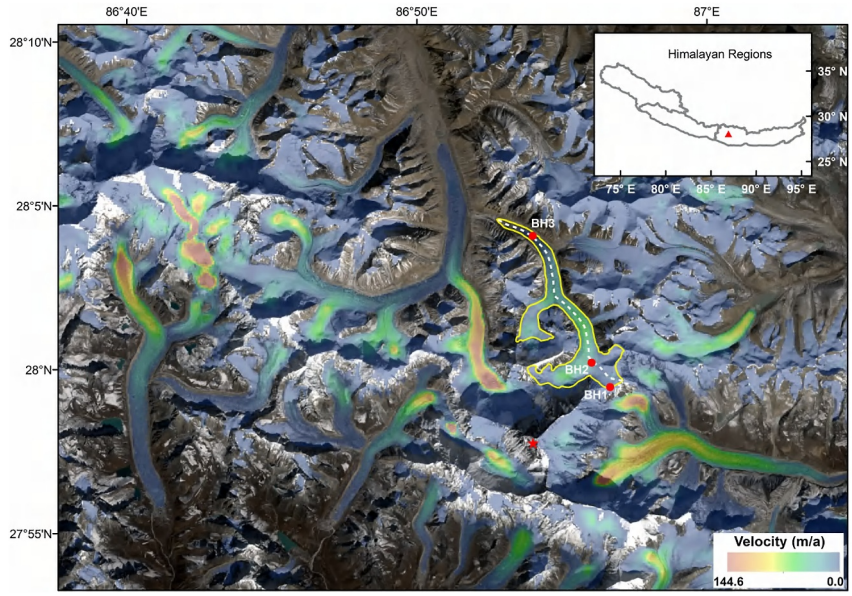

Figure 1. ERG location in the Everest Region. The glacier outline is in yellow. The inset plot shows the location of the ERG (red triangle) in the Himalaya mountain range. The background image is a panchromatic Landsat 8 scene on 13 November 2014, overlaid with the ITS-LIVE ice velocity product. BH1, BH2, and BH3 denote three shallow borehole locations (Zhang et al., 2013). The white dashed line is the central flowline. The red star is the summit of Mt. Everest.

Currently, there have been a few studies regarding future glacier projections in HMA. Some of them use ice flow models with high numerical complexities. For example, a three-dimensional, full-Stokes thermomechanical model was applied to simulate the evolution of the Gurenhekou glacier, southern Tibetan Plateau, by parameterizing the temperature and surface mass-balance (SMB) uncertainties (L. Zhao et al., 2014). Using the same ice flow model, the evolution of Da Anglong Glacier, western Tibetan Plateau, was simulated from 2016 to 2098 based on projected temperatures and precipitation from the 25-km-resolution RegCM4 under the RCP2.6 and RCP8.5 scenarios (W. Zhao et al., 2022). But there are also other studies that did not explicitly include robust ice dynamics for modeling mountain glaciers (Gao et al., 2021; Khadka et al., 2020; Kraaijenbrink et al., 2017; Rounce et al., 2020; Shea et al., 2015). In addition, for most of individual glacier projection studies in HMA, they do not include model validations against observations of past glacier changes, and also do not explore clearly the relative importance of the impacts of ice dynamics and surface mass balance on glacier changes (L. Zhao et al., 2014; Gao et al., 2021). This causes a lack of confidence regarding promoting individual glacier modeling efforts to basin-scale glacier change studies in HMA.

To better understand these dynamic processes and uncertainties, we select East Rongbuk Glacier (ERG) on the northern slope of Mt. Everest (Figure 1), and investigate its recent changes to provide useful process-level insight on the future of HMA glaciers. In recent decades, Mt. Everest experienced an atmospheric warming trend of approximately 0.033 K a^{-1}, and glaciers in the region are shrinking (Kang et al., 2022). On the southern slope of Mt. Everest, Shea et al. (2015) found 20% decrease in glacier area during 1961–2007. Thakuri et al. (2014) and King et al. (2020) examined glacier changes in the Mt. Everest region for the last five to six decades using remote sensing methods. However, ice dynamic studies of Mt. Everest's northern slope are still lacking. In the past several decades, a few field expeditions have been conducted on ERG, and some necessary glaciological data sets for ice modeling studies, for example, ice thickness and temperature, have been collected (Zhang et al., 2013). Previously, a simplified, two-dimensional (2D) modeling study discovered a polythermal structure along the main flowline of ERG (Zhang et al., 2013), but the basal slip condition was poorly constrained due to the lack of a robust basal friction inversion algorithm.

This paper is organized as follows. First, we briefly introduce the numerical modeling approaches for our experiments, including the 3D first-order ice flow model and the Robin inversion procedure. Then, we describe the data we use for modeling ERG. Next, we investigate the thermomechanical changes of ERG during 2010–2100, and finally following the discussions and conclusions of the paper.

2. Model Descriptions

2.1. The First-Order (Blatter-Pattyn) Ice Flow Model

The numerical framework of our 3D ice flow model is the same as in our previous Stokes model studies (Leng et al., 2012; Zhang et al., 2017), but with a different first-order approximation (Yan et al., 2022), where the momentum balance equations for the first-order approximation can be expressed as in Perego et al. (2012) and Hoffman et al. (2018),

$$\begin{aligned} -\nabla\cdot\left(2\eta\dot{\boldsymbol{\epsilon}}_1\right)+\rho g\frac{\partial H_s}{\partial x}=0,\\ -\nabla\cdot\left(2\eta\dot{\boldsymbol{\epsilon}}_2\right)+\rho g\frac{\partial H_s}{\partial y}=0, \end{aligned} \tag{1}$$

where x and y are the horizontal coordinate vectors in a Cartesian reference frame, $s(x, y)$ is the ice surface elevation, and $\dot{\boldsymbol{\epsilon}}_1$ and $\dot{\boldsymbol{\epsilon}}_2$ are strain rates given by

$$\begin{aligned} \dot{\boldsymbol{\epsilon}}_1&=\left(2\dot{\epsilon}_{11}+\dot{\epsilon}_{22},\dot{\epsilon}_{12},\dot{\epsilon}_{13}\right)^T,\\ \dot{\boldsymbol{\epsilon}}_2&=\left(\dot{\epsilon}_{12},\dot{\epsilon}_{11}+2\dot{\epsilon}_{22},\dot{\epsilon}_{23}\right)^T, \end{aligned} \tag{2}$$

where $\dot{\epsilon}_{ij}(i,j=1,2,3)$ are the corresponding strain-rate components. The viscosity of ice (η) can be calculated as in Cuffey and Paterson (2010),

$$\eta=\frac{1}{2}A^{-\frac{1}{n}}\dot{\epsilon}_e^{\left(\frac{1}{n}-1\right)}, \tag{3}$$

where the temperature-dependent rate factor $A(T)$ is described by the Arrhenius law,

$$A(T)=A_0e^{-Q/RT}, \tag{4}$$

where T is the ice temperature in Kelvin (K), A_0 is the preexponential constant, Q is the activation energy, and R is the universal gas constant. The effective strain rate $\dot{\epsilon}_e$ is defined as

$$\dot{\epsilon}_e\equiv\left(\dot{\epsilon}_{11}^2+\dot{\epsilon}_{22}^2+\dot{\epsilon}_{11}\dot{\epsilon}_{22}+\dot{\epsilon}_{12}^2+\dot{\epsilon}_{13}^2+\dot{\epsilon}_{23}^2\right)^{\frac{1}{2}}. \tag{5}$$

The stress-free boundary condition at the upper surface can be described as

$$\dot{\boldsymbol{\epsilon}}_1\cdot\mathbf{n}=\dot{\boldsymbol{\epsilon}}_2\cdot\mathbf{n}=0, \tag{6}$$

where $\mathbf{n}$ is the outward-pointing normal vector at the ice surface. At the ice base, we apply a linear sliding law

$$\mathbf{u}\cdot\mathbf{n}=0,\qquad 2\eta\dot{\boldsymbol{\epsilon}}_1\cdot\mathbf{n}+\beta\mathbf{u}_1=0,\qquad 2\eta\dot{\boldsymbol{\epsilon}}_2\cdot\mathbf{n}+\beta\mathbf{u}_2=0, \tag{7}$$

where β is a positive value of the basal friction coefficient (Pa a m^{-1}).

2.2. Ice Temperature Model

The conservation of energy is expressed through the advective/diffusive heat equation,

$$\rho c\left(\frac{\partial T}{\partial t}+\boldsymbol{u}\cdot\nabla T\right)=k\nabla^2T+2\eta\dot{\boldsymbol{\epsilon}}:\dot{\boldsymbol{\epsilon}}, \tag{8}$$

Table 1
Model Constants Used in Our Experiments

Symbol	Description	Value	Units
ρ	Ice density	910	kg m^{-3}
c	Heat capacity of ice	2,009	J $kg^{-1}K^{-1}$
g	Gravitational constant of acceleration	9.81	m s^{-2}
n	Flow law exponent	3	–
A_0	Pre-exponential constant	3.985×10^{-13} ($T \leq 263.15$ K)	s^{-1} Pa^{-3}
		1.916×10^{3} ($T \geq 263.15$ K)	s^{-1} Pa^{-3}
Q	Activation energy	60 ($T \leq 263.15$ K)	kJ mol^{-1}
		139 ($T \geq 263.15$ K)	kJ mol^{-1}
k	Thermal conductivity of ice	2.1	W $m^{-1}K^{-1}$
α	Clausius–Clapeyron constant	8.7×10^{-4}	K m^{-1}
γ_e	Lapse rate	−7.2	K km^{-1}

where k is the conductivity and c is the heat capacity of ice (taken as constants here). At the ice surface, a Dirichlet-type boundary condition is applied, that is, $T = T_s$, where T_s is the ice surface temperature. In this study, we set T_s to the borehole temperature T_{BH} at the shallow borehole drilling sites, as a proxy of annual mean air temperature at ice surface. At the ice base, we use a Neumann-type condition,

$$G = -k\frac{\partial T}{\partial z}, \tag{9}$$

where G represents the geothermal heat flux at the ice-bedrock interface. Additionally, for all of our model experiments, the ice temperature is not allowed to exceed the pressure-melting temperature of ice (an approximation of energy conservation when both englacial water content and temperate ice zone is small),

$$T \leq T_{\text{pmp}}, \tag{10}$$

where the pressure-melting-point of glacier ice (T_{pmp}) is described by the Clausius-Clapeyron relation

$$T_{\text{pmp}}(z) = T_0 - \alpha(s - z), \tag{11}$$

where T_0 is the triple point of water, s is the ice surface elevation, and α is the Clausius-Clapeyron constant.

2.3. Mass Conservation

The glacier mass transport and evolution is simulated according to mass conservation law. The ice density is assumed as a constant, and then the glacier thickness evolution can be described as follows, the equation relates ice thickness change to the divergence of mass and sources and sinks:

$$\frac{\partial H}{\partial t} + \nabla \cdot H\bar{\mathbf{u}} = B, \tag{12}$$

where H is ice thickness, t is time, $\bar{\mathbf{u}}$ is depth-averaged velocity, and B is surface mass balance. As the basal melt for ERG is very small, it is neglected in this study. All constants used in this study can be found in Table 1.

2.4. Robin-Type Inversion

Following Arthern and Gudmundsson (2010) and Arthern et al. (2015), we solve for the basal friction coefficient β using the Robin inversion algorithm by iteratively minimizing the cost function J across the basal domain based on a given 3D temperature field

$$J = \int_{\Gamma_b} \beta \left| \boldsymbol{u}^D - \boldsymbol{u}^N \right|^2 \, \mathrm{d}S, \tag{13}$$

where $\boldsymbol{u}^D$ and $\boldsymbol{u}^N$ are the observed (Dirichlet-type) and modeled (Neumann-type) ice surface velocities, respectively. This cost function represents the mismatch between the Neumann and Dirichlet velocity fields. According to Arthern et al. (2015), the basal friction coefficient was updated as follows:

$$\beta_{n+1}(x,y) = \beta_n(x,y) + \alpha_\beta \left(\left| \mathbf{u}_b^N \right|^2 - \left| \mathbf{u}_b^D \right|^2 \right), \tag{14}$$

where α_β is a positive parameter that determines the step size, which is given as

$$\alpha_\beta = \frac{\beta_n}{\left| \mathbf{u}_b^D \right|^p} \frac{\left(\left| \mathbf{u}_b^N \right|^p - \left| \mathbf{u}_b^D \right|^p \right)}{\left(\left| \mathbf{u}_b^N \right|^2 - \left| \mathbf{u}_b^D \right|^2 \right)}, \tag{15}$$

where p is a positive parameter. For all numerical experiments, we set p as 1.5. To invert both the basal temperature and friction, we adopt a similar approach as in Seddik et al. (2019) following these steps:

1. Assuming a no-slip boundary condition at the ice base and a stress-free (Neumann) boundary condition at the ice surface, we solve the diagnostic, thermomechanical steady state of the ERG;
2. Using the 3D temperature field from the previous step, the Robin inversion is conducted by setting the Dirichlet boundary condition using the ITS_LIVE ice surface velocity data and obtaining an initial guess of the basal friction parameter β;
3. Using the β value from the previous step, we turn on the basal slip in the code and obtain an updated ice temperature field;
4. Repeat step (2.) and update β;
5. Repeat step (3.) and update the 3D ice temperature field.

We take the ice temperature field from step (5.) as the final output. In our Robin inversion procedures, we do not invert basal friction and ice viscosity simultaneously, but instead separate them in an iterative manner. We therefore do not apply the regularization term as in Jay-Allemand et al. (2011), but use the stopping criterion of stagnant cost function, similar to Arthern and Gudmundsson (2010) and Arthern et al. (2015).

3. Data

3.1. Glacier Geometry

For 3D ice geometry, we combine both in situ and modeled GlaTE (Glacier Thickness Estimation) data. In May 2009, a ground penetrating radar (GPR) survey was conducted on the ERG. A detailed description of the GPR survey and ice thickness data can be found in Zhang et al. (2013). Due to large ice seracs and heavily crevassed regions, a large portion of the ERG area still lacks in situ ice thickness data. Here, we use the GlaTE data to estimate the ERG ice thickness distribution (Langhammer et al., 2019). The GlaTE framework infers thickness distribution by combining glaciological modeling results with GPR measurements. The glaciological model of GlaTE follows the bed stress approach proposed by Clarke et al. (2013). To estimate the distributed ice thickness, glacier outline and surface topography are required as inputs for GlaTE. We manually delineated the ERG glacier outline from Landsat-7 ETM + imagery (Figure 1). As for surface topography, we use the AW3D30 DEM (ALOS World 3D-30 m) generated from multiple stereo images with a mean date in April 2009 (Tadono et al., 2014) (Figure 2a). The performance of GlaTE depends on the observations available for model calibration. As there were very few in situ ice thickness measurements in the accumulation zone and lateral regions away from the center flowline, the inferred ice geometry remains uncertain and may also introduce model uncertainties in these regions. The 2020 ice surface geometry is inferred from 2010 to 2020 elevation change data in Hugonnet et al. (2021).

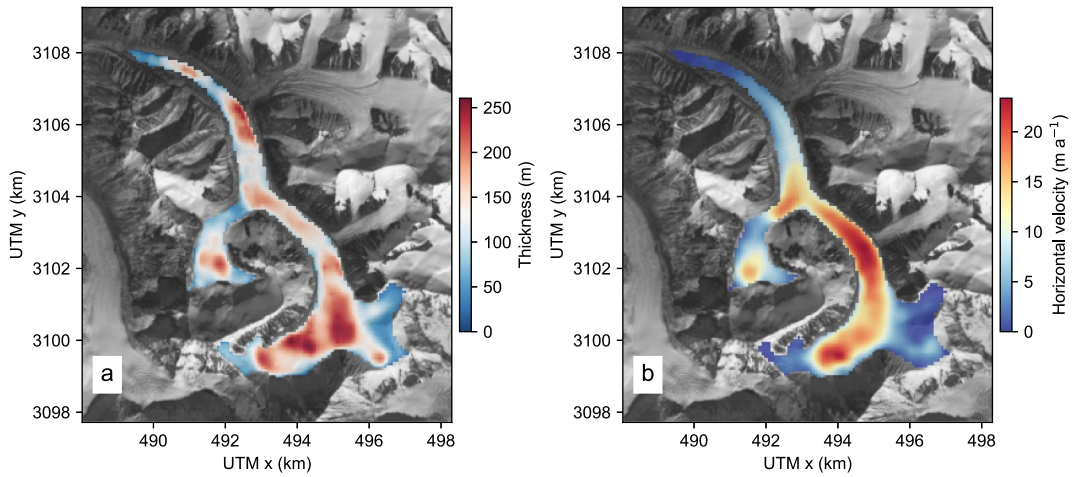

Figure 2. Spatial distribution of the ice thickness (a) and horizontal surface velocity (b) of ERG in 2009. The background image is same as in Figure 1.

3.2. Ice Borehole Temperature

At ERG, in situ observed ice temperature data are rare. The most recent ice boreholes for temperature measurements were drilled at an elevation of 6350 m a.s.l. (BH2) and 5710 m a.s.l. (BH3), in 2011. At BH2, we measured an ice temperature of −1.9°C at a depth of 18.5 m. At BH3, we measured an ice temperature of −7.1°C at a depth of 10 m. Despite these few in situ measurements indicating ice temperatures well below the pressure-melting-point, our previous study speculated from ice-penetrating radar that large valley glaciers in the Mt. Everest region likely sustained temperate ice zones (TIZs) in the basal ice of their ablation zones (Zhang et al., 2013).

3.3. Ice Surface Velocity

We use the NASA MEaSUREs ITS_LIVE surface ice velocity product from 2009 to infer basal friction parameters. The ITS_LIVE data product is derived from Landsat 4, 5, 7, and 8 imagery using a feature-tracking approach (Gardner et al., 2019). Although the ITS_LIVE data provides yearly ice velocity products spanning a time period from 1985 to 2018, the grid resolution is 240 m, which is relatively coarse for our ice flow modeling study. The surface velocity components v_x (east-west direction) and v_y (north-south direction) are generated by ITS_LIVE. All these surface velocities are resampled to 90 m resolution using bilinear interpolation method in order to be consistent with the geometry data (Figure 2b).

3.4. Surface Mass Balance

In situ surface mass balance observations at ERG are also scarce. They were mostly obtained during the time period 2006–2011, spanning an elevation range of 5780–6480 m a.s.l. (Figure 3). In this study, we parameterize the surface mass balance by the following relationship

$$B = \gamma_1 (h_s - h_{ELA}) \tag{16}$$

where h_{ELA} is the elevation of equilibrium line of altitude (ELA) and the gradient γ_1 is 0.00455. In addition, the variation of the ELA with the change in air temperature can be expressed as in Colgan et al. (2012),

$$\Delta h_{ELA} = \Delta T_S / \gamma_T, \tag{17}$$

where γ_T represents the air temperature lapse rate, which is set to a constant of −0.0072°C m^{-1} (Zhang et al., 2013), ΔT_S is the change of surface air temperature relative to the initial year (2009) on ERG, and Δh_{ELA} represents the annual change in ELA. The ELA at 2009 is obtained from in situ observations and Landsat 7 image.

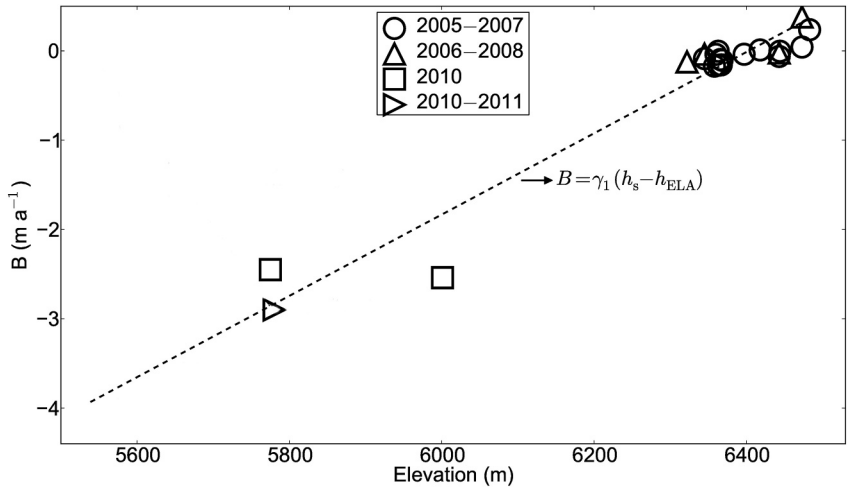

Figure 3. Surface mass balance (B) observations, and their parameterization on ERG. These are in situ data obtained during 2005–2011. γ_1 is the surface mass balance gradient, h_s is the ice surface elevation and h_{ELA} is the elevation at the equilibrium line of altitude.

3.5. Climate Forcing

We use bias-corrected annual climate forcing data sets from CMIP6 with 10 GCMs and 3 climate scenarios (SSP126, 370 and 585), which are obtained from the Inter-Sectoral Impact Model Intercomparison Project Phase 3b (ISIMIP3b). A detailed description of the climate forcing data preparation can be found in H. Zhao et al. (2023). In this study, we use the GCM temperature data to adjust the ELA changes and parameterize SMB profiles during our model runs.

4. Numerical Experiments

The accuracy of future projections by an ice flow model depends on the accuracy of a number of boundary conditions. At model initialization, the diagnostic Robin inversion method takes observed ice surface velocity and glacier topography as inputs, and it also relies on a plausible ice temperature field. During the prognostic model runs, the SMB forcing data becomes more critical.

For model initialization, we take the ice velocity and geometry data as model inputs, and do not consider their uncertainties. Instead, we consider the major model uncertainty that arises from the thermal boundary conditions at the ice surface and ice-bedrock interface. For ERG, a low geothermal heat flux value (approximately 19 mW m^{-2}) was inferred from the in situ ice temperature gradient in a 108 m borehole at the ice divide (Zhang et al., 2013). However, as this borehole was located at the glacier margin at a high elevation of approximately 6500 m a.s.l., the corresponding geothermal heat flux data may very likely underestimate the basal heat flow of ERG across the whole model domain.

In addition, despite relatively easy access to observed or reanalyzed air temperature data for HMA glaciers, these air temperatures are not always equivalent to ice surface temperature as the upper thermal boundary condition. Mean annual air temperature can be estimated from the 10 m or 15 m near-surface temperature at cold and dry surfaces (Cuffey & Paterson, 2010). However, for regions where meltwater refreezing occurs, the near-surface temperature may be higher than the mean annual air temperature (Gilbert et al., 2014; Wang et al., 2018). Therefore, the near-surface ice temperature is generally a better proxy for the upper thermal boundary condition.

To investigate the uncertainties raised by both upper and lower thermal boundary conditions, we tested three different geothermal heat flux values, that is, 20, 30, and 40 mW m^{-2}, representing lower, medium and higher values for the basal thermal boundary condition. Further, we use the borehole temperature at BH2 (T_{BH2}, 18.5 m deep) and BH3 (T_{BH3}, 10 m deep), respectively, to parameterize the mean annual ice surface temperature at different ice elevations,

Table 2
Six Numerical Experiments for Exploring the Uncertainties of Thermal Boundary Conditions

	Expt (a)	Expt (b)	Expt (c)	Expt (d)	Expt (e)	Expt (f)
G(mW m^{-2})	20	30	40	20	30	40
T_{BH}(°C)	−7.1	−7.1	−7.1	−1.9	−1.9	−1.9
z_{BH}(m a.s.l.)	6350	6350	6350	5710	5710	5710
A_{2009}(km^2)	0.0076	0.14	0.45	0.09	0.41	0.83

Note. G is the geothermal heat flux. T_{BH} and z_{BH} are the ice temperature and elevation of the borehole. A_{2009} is the area of basal temperate ice region for 2009 inferred by our ice flow model.

$$T_s = T_{BH} + \gamma_e (z - z_{BH}), \tag{18}$$

where γ_e is the environmental lapse rate, z is the ice surface elevation, T_{BH} and z_{BH} are the near-surface borehole temperatures and their elevations, respectively. We list the parameters of 6 numerical experiments in Table 2. Through this approach we consider the sensitivity of englacial thermal regime to both the upper and lower thermal boundary conditions. Therefore, we design six diagnostic sensitivity experiments (a)–(f) for 2009 using the surface temperature settings and the geothermal heat flux values, as shown in Table 2.

In the prognostic simulations, we consider three different model approaches: (a) parameterize SMB using the CMIP6 temperature data and assume the SMB gradient remains the same during model runs, denoted as "SMBg"; (b) use both CMIP6 temperature and precipitation data to calculate SMB as in H. Zhao et al. (2023), denoted as "SMBp"; (c) same as "SMBp" but turning off ice dynamics, denoted as "nDyn." By this experiment design, we can understand how different climate forcings impact ERG changes in the future, and specifically isolate the importance of ice flow dynamics in the evolution of ERG.

5. Results and Discussions

5.1. Model Initialization

By Robin inversion, the discrepancy between the modeled and observed ice surface velocities decreases rapidly within only a few iterations. The modeled 2009 ice surface velocity results for the six diagnostic experiments are shown in Figure 4. Their differences than the observed ice surface velocity are shown in Figure 5. These simulations can all generally reproduce the observed spatial pattern of ice surface velocity, that is, large ice surface velocities in the up- and mid-stream regions (20–30 m a^{-1}), but very slow motion (close to stagnant) near the glacier terminus.

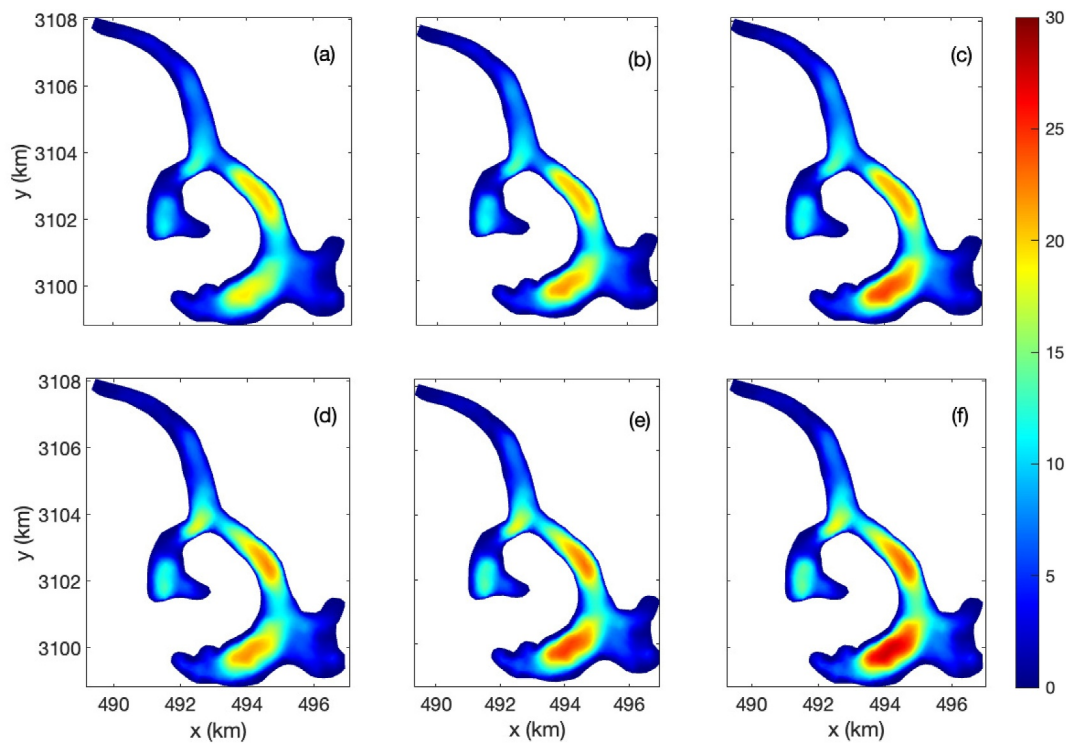

Figure 4. The modeled ice surface velocity (m a^{-1}) in 2009 for six diagnostic numerical sensitivity experiments (a)–(f).

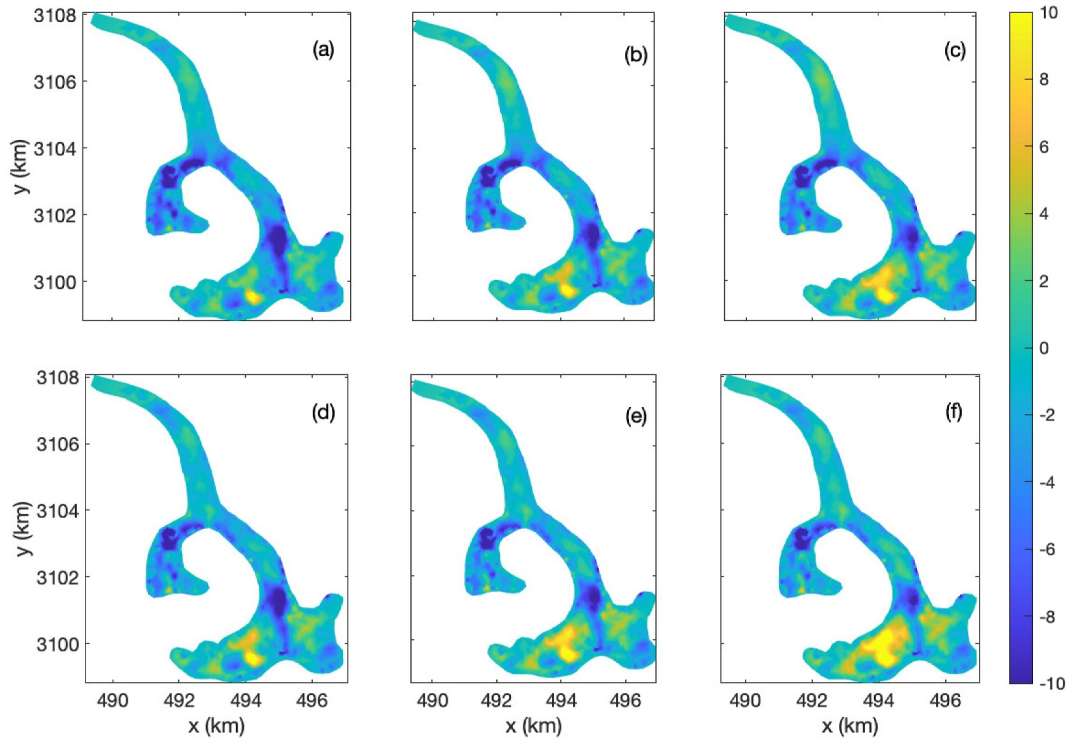

Figure 5. The differences between modeled and observed ice surface velocity ($u_{mod} - u_{obs}$, m a^{-1}) in 2009 for six diagnostic numerical sensitivity experiments (a)–(f).

From linear regression between modeled and observed ice surface velocities for these six experiments (Figure 6), we can clearly see that our Robin inversion algorithm robustly reproduces the observed ice speed for ERG ($r^2 > 0.9$). Across these six experiments, we can see that the modeled ice surface velocities are different from each other. In general, compared to observations, the ice surface velocities of cold scenarios Expt (a) and (d) show slightly better agreements than those for warmer scenarios, Expt (c) and (f). For example, Expt (f) appears to have more locations that overestimate the ice surface velocities, especially in the accumulation area.

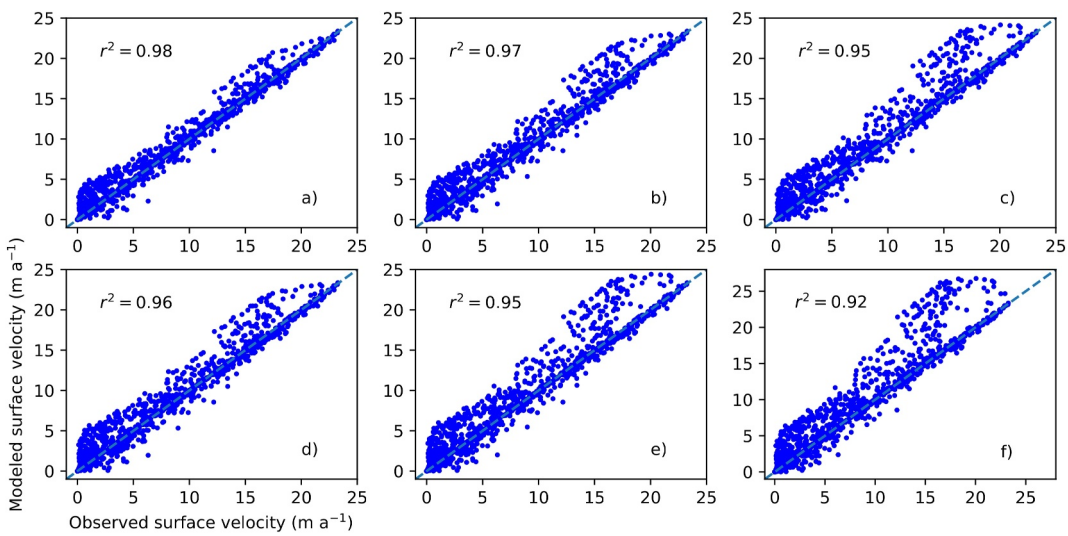

Figure 6. Linear regression between modeled and observed ice surface velocity data in 2009 for six diagnostic experiments (a)–(f).

10.1029/2024EF004545

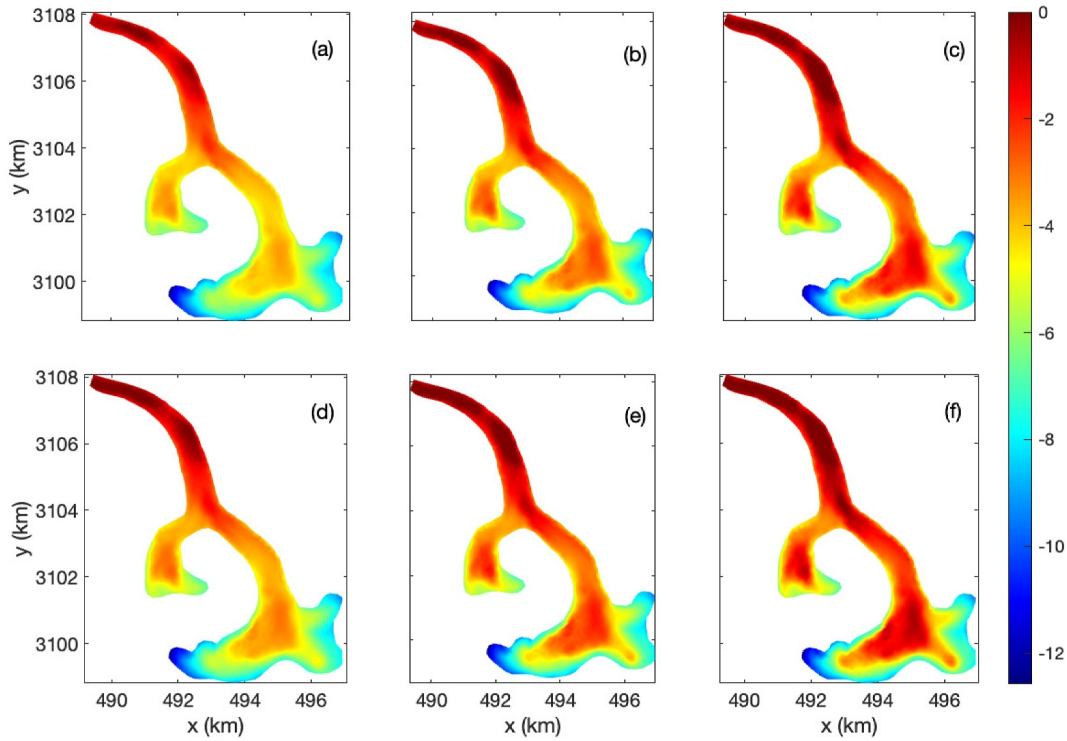

Figure 7. The spatial distribution of basal ice temperature relative to pressure melting point ($T - T_{pmp}$) (°C) in 2009 for six diagnostic sensitivity experiments (a)–(f). The temperate ice regions can be clearly recognized by $T - T_{pmp} = 0$°C.

The basal ice temperature distribution of the six experiments is shown in Figure 7. In these simulations, the basal ice becomes warmer if we increase the geothermal heat flux or use T_{BH3} to parameterize the ice surface temperature as the upper thermal boundary condition. In general, we can see that more basal temperate ice appears from Expt (a) to Expt (f) (Table 2). Take the 2009 model results for instance. For Expt (a), there is only a very small area (0.0076 km^2) of basal ice that reaches the pressure melting point. This temperate ice area increases to 0.14 and 0.45 km^2 when we increase the geothermal heat flux to 30 mW m^{-2} (Expt b) and 40 mW m^{-2} (Expt c), respectively. If we apply a warmer surface thermal boundary condition, the basal ice area that reaches the pressure melting point is 0.09 km^2 (Expt d), 0.41 km^2 (Expt e), and 0.83 km^2 (Expt f).

In Figure 7, we can see that for all of our sensitivity experiments, the basal temperate ice regions with various size appear in the downstream, ablation part of ERG even for the coldest settings (Expt a), where both the surface slope and ice velocity are generally small. The accumulation area of ERG is, however, still cold-based. This pattern is similar to the results of our previous 2D modeling study (Zhang et al., 2013). Our 3D model efforts here provide stronger evidence of the existence of basal temperate ice on ERG.

If we compare the extent of modeled basal temperate ice region in 2009 to the in situ ground penetrating radar measurements in Zhang et al. (2013), we find some consistency and agreement. For example, in Figures 2 and 9 in Zhang et al. (2013), we can see that the grounding penetrating radar survey line L2 (see Figure 1 in Zhang et al. (2013)) is close to BH3 and presents some obscure radar signal reflection features at the bottom, probably indicating the existence of basal temperate ice. A parallel but much longer survey line L1 (see Figure 1 in Zhang et al. (2013)) also shows some similar but discontinuous temperate ice signals. This is now qualitatively supported by the modeled temperate ice extent in Expts b, c, e, and f in this study.

5.2. Future Projections

Similar to other higher-order ice flow modeling studies (Hoffman et al., 2018), we perform a 5-year relaxation with evolving velocity and geometry from the initialized state. After that, based on the inversion procedure in the previous step, we choose the thermal boundary conditions from Expt (a) as the best match between modeled and observed ice surface velocities (Figure 6) for the future projection experiments. Note that in our future projections

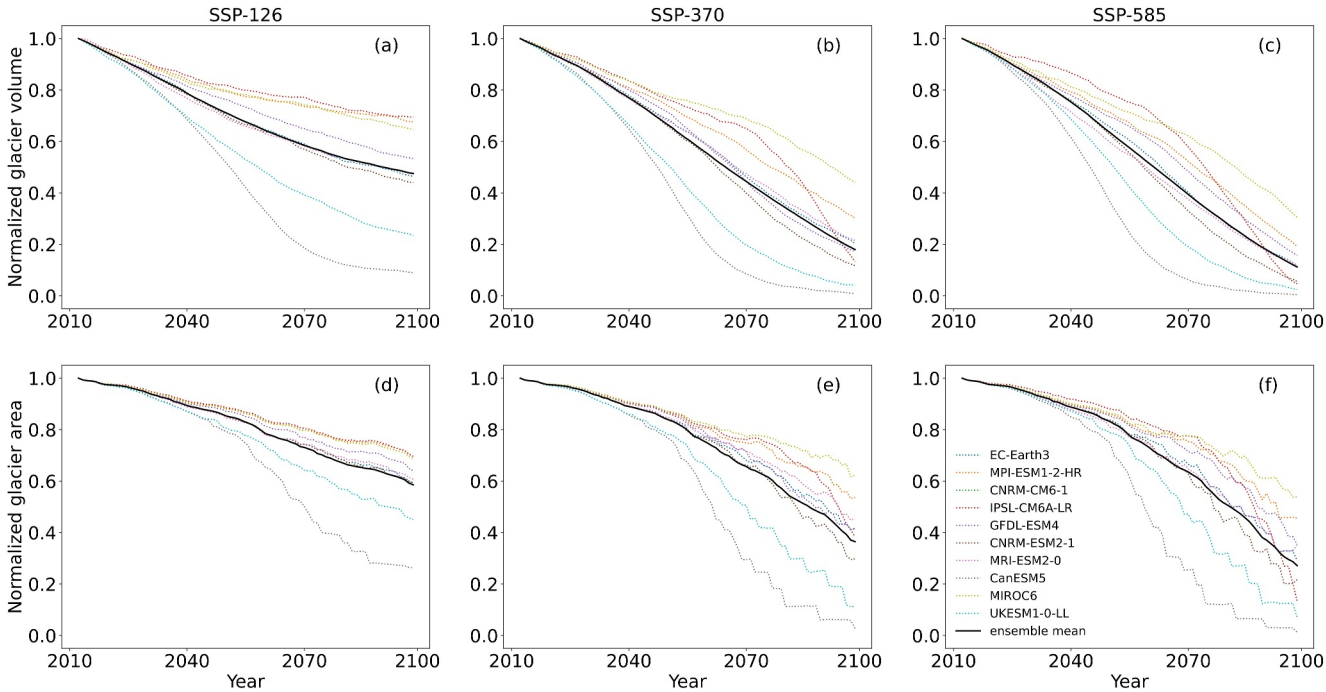

Figure 8. (a)–(c) Normalized cumulative volume changes of ERG during 2010–2100. (d)–(f) Normalized cumulative area changes of ERG during 2010–2100. The dotted thin lines are individual simulations for different CMIP6 forcings. The solid thick lines are the ensemble means. The first, second and third column represent for SSP-126, SSP-370, and SSP-585, respectively.

the inverted basal friction is kept constant in time, which is a common approach adopted in ice flow models (Seroussi et al., 2019). Here we drive our ice flow model with 10 CMIP6 climate model forcings (surface air temperature) and also their ensemble mean by parameterizing the surface mass balance at ERG. In Figure 8 we show the modeled changes of normalized ice volume (Figure 8a) and area (Figure 8b) during 2010–2100 for three CMIP6 climate scenarios, SSP-126, SSP-370, and SSP-585.

Similar to previous HMA glacier runoff studies like Rounce et al. (2020) and H. Zhao et al. (2023), our results also show a continuous trend of glacier mass loss. But the temporal pattern is a bit different. From Rounce et al. (2020), where no ice dynamics are considered, we see that the change rate of total glacier mass for central Himalaya gets smaller in time (Figure 3 in Rounce et al. (2020)), but in this study our ensemble mean curves show that the change rates for ice volume will first increase and then decrease in the next 80 years. For SSP 370 and 585, the volume change rate at around 2050 (0.023 $km^3\ a^{-1}$) will reach 1.5 times than that at around 2010 (0.015 $km^3\ a^{-1}$). Our results here are more similar to that in H. Zhao et al. (2023) which used a model including very simple ice dynamics module (Shallow Ice Approximation). This underlies the importance of considering ice flow in estimating the changes of basin-scale mountain glaciers in the future.

Ice dynamics appear to be unimportant at the beginning of the projection period, but their role in accelerating ice loss magnifies in time (Figure 9). The remaining ice volume for the nDyn case is around 110%, 125% and 135% larger than the SMBp and g cases at the year 2100 for SSP-126, SSP-370 and SSP-585, respectively. This indicates that ice dynamics play a bigger role in affecting ice mass changes as climate gets warmer (W. Zhao et al., 2022). As ice flows faster, the ice mass from upstream will be more easily transported to the ablation region at downstream. However, the glacier area generally shows an opposite pattern, that is, the glacier area for the nDyn cases shrinks more rapidly compared to the other two experiments. This is because glacier dynamics transport ice mass from upstream to downstream, delaying the shrinkage of glacier area. This highlights a deficiency in monitoring glacier change by just measuring area. The SMBp and SMBg experiments show close simulation results, possibly implicating that temperature is a more dominant function than precipitation in parameterizing glacier surface mass balance and the SMBg method is applicable at least in this study.

10.1029/2024EF004545

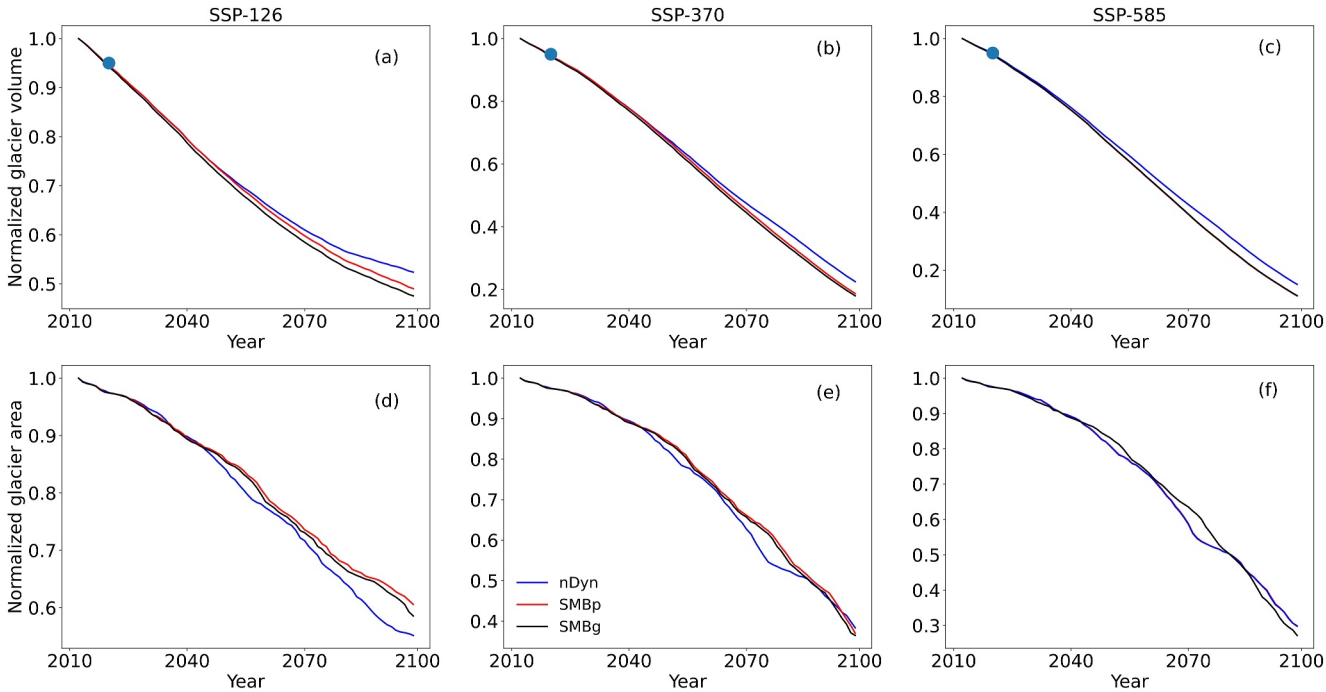

Figure 9. (a)–(c) Normalized cumulative volume changes of ERG during 2010–2100. (d)–(f) Normalized cumulative area changes of ERG during 2010–2100. The blue curves represent experiments that do not include ice dynamics. The red and black curves represent two different surface mass balance parameterizations. The solid thick lines are the ensemble means. The first, second and third column represent for SSP-126, SSP-370, and SSP-585, respectively. The solid circle represents the observed normalized ice volume in 2020.

We should note that our model is able to well capture the observed ice volume loss during 2010–2020 (Figure 9). From Hugonnet et al. (2021) we know the 2010–2020 elevation changes at ERG. We can then calculate the ice loss of around 0.094 km^3, that is, 4.75% of the total ice volume. In the same period of time, our modeling results show that ERG volume decreases by around 0.1 km^3 for three climate scenarios, SSP-126, SSP-370 and SSP-585. This lends us great confidence in the accuracy of our model performance.

Moreover, in Figure 10 we also present the ice mass loss (ΔV) for each year during our model time span. Clearly, the ΔV values show a trend of first increasing and then decreasing after ERG reaches the turning point of peak water runoff. Note that, in this study, we define the glacier runoff as the net glacier mass loss (Radić & Hock, 2014), which is a different concept than that only considers the ice surface melt, and emphasizes the contribution of glaciers to the hydrological cycle (Huss, 2011). The warmer climate scenario has a stronger driver to melt ERG and maintain a longer period of higher level glacier runoff. For SSP-126, the peak water is likely to occur at the year 2030, while for SSP-370 and 585, their peak water occur at the year 2060 and 2059, respectively.

The timings of peak water runoff between our single ERG case and basin-scale projections are also different. In Rounce et al. (2020) and H. Zhao et al. (2023), the peak water for the Brahmaputra river basin, where ERG is located, occurs before 2030 for all climate scenarios. The Brahmaputra river basin (shown in H. Zhao et al. (2023)) contains many maritime-type glaciers in the southeastern region of the Tibetan Plateau (Huss & Hock, 2018; Rounce et al., 2020). The fast flow and strong ablation of maritime glaciers may lead to an early timing of peak water (Han et al., 2023), different from the Mt. Everest region, where the climate is mainly dry and the glaciers generally move slowly. This pattern can also be recognized for the Qiangtang drainage basin, where the climate condition is also continental type and the timings of peak water are generally later than that for the Brahmaputra river basin (H. Zhao et al., 2023).

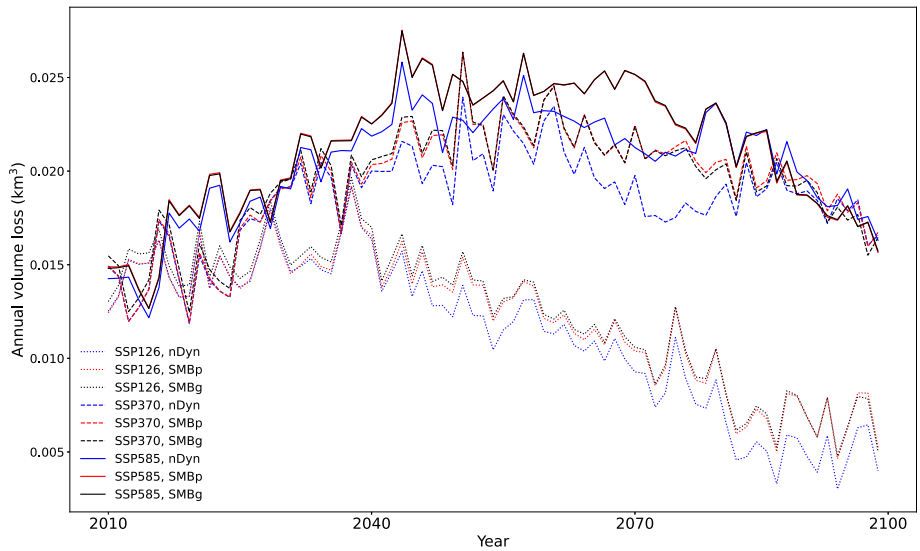

Figure 10. Normalized annual ice volume changes (ensemble mean) for SSP-126 (blue), SSP-370 (red), and SSP-585 (black). The dotted, dashed and solid lines are for non-dynamical and two surface mass balance parameterization methods, respectively.

6. Conclusions

East Rongbuk Glacier (ERG), Mt. Everest, is one site within HMA that has relatively well surveyed in situ glaciological data. Thus, a projection of meltwater changes at ERG using a three-dimensional model with high numerical complexity is necessary to further understand the HMA glacier changes expected this century. In this study, we conduct 6 diagnostic sensitivity experiments regarding basal and surface thermal boundary conditions to better constrain our model initialization. For prognostic simulations, we consider two different surface mass balance forcing schemes. We also run simulations that do not include glacier dynamics (only surface mass balance).

The model results suggest again the existence of a basal temperate ice zone, similar to previous studies. We find the existence of temperate basal ice even for the coldest model settings. The most likely location of temperate ice is at approximately 5700–5800 m a.s.l., where a high near-surface temperature was observed in a shallow borehole. From our prognostic experiments, we find ERG will continuously loss mass this century. For the SSP-126 scenario, ERG may likely produce peak annual meltwater runoff at 2030, while for SSP-370 and SSP-585, the peak meltwater runoff timing is around at 2060. We also find that ice dynamics become non-trivial as climate gets warmer, and as model time increases, indicating the importance of considering glacier dynamics that are generally missing from current HMA large-scale glacier modeling efforts.

Conflict of Interest

The authors declare no conflicts of interest relevant to this study.

Data Availability Statement

The AW3D30 DEM data is given by Tadono et al. (2014). The ice surface velocity ITS_LIVE is available in Gardner et al. (2019). The geometry and projection data of East Rongbuk Glacier in this study can be obtained from Zhang et al. (2024).

Acknowledgments
This work was supported by Open Research Fund of TPESER, Grant TPESER202203, the National Natural Science Foundation of China Grants 42271133 and 42271134, and the State Key Laboratory of Earth Surface Processes and Resource Ecology (2022-ZD-05), and the Beijing Normal University Talent Introduction Project of China (12807-312232101). We thank two anonymous reviewers and the editor Noah Diffenbaugh for the great improvements of this paper.

References

Arthern, R. J., & Gudmundsson, G. H. (2010). Initialization of ice-sheet forecasts viewed as an inverse Robin problem. *Journal of Glaciology*, *56*(197), 527–533. https://doi.org/10.3189/002214310792447699

Arthern, R. J., Hindmarsh, R. C., & Williams, C. R. (2015). Flow speed within the Antarctic ice sheet and its controls inferred from satellite observations. *Journal of Geophysical Research: Earth Surface*, *120*(7), 1171–1188. https://doi.org/10.1002/2014jf003239

Azam, M. F., Kargel, J. S., Shea, J. M., Nepal, S., Haritashya, U. K., Srivastava, S., et al. (2021). Glaciohydrology of the Himalaya-Karakoram. *Science*, *373*(6557), eabf3668. https://doi.org/10.1126/science.abf3668

Barnett, T. P., Adam, J. C., & Lettenmaier, D. P. (2005). Potential impacts of a warming climate on water availability in snow-dominated regions. *Nature*, *438*(7066), 303–309. https://doi.org/10.1038/nature04141

Bhattacharya, A., Bolch, T., Mukherjee, K., King, O., Menounos, B., Kapitsa, V., et al. (2021). High Mountain Asian glacier response to climate revealed by multi-temporal satellite observations since the 1960s. *Nature Communications*, *12*(1), 1–13. https://doi.org/10.1038/s41467-021-24180-y

Clarke, G. K. C., Anslow, F. S., Jarosch, A. H., Radić, V., Menounos, B., Bolch, T., & Berthier, E. (2013). Ice volume and subglacial topography for western Canadian glaciers from mass balance fields, thinning rates, and a bed stress model. *Journal of Climate*, *26*(12), 4282–4303. https://doi.org/10.1175/JCLI-D-12-00513.1

Colgan, W., Rajaram, H., Anderson, R. S., Steffen, K., Zwally, H. J., Phillips, T., & Abdalati, W. (2012). The annual glaciohydrology cycle in the ablation zone of the Greenland ice sheet: Part 2. Observed and modeled ice flow. *Journal of Glaciology*, *58*(207), 51–64. https://doi.org/10.3189/2012JoG11J081

Cuffey, K., & Paterson, W. (2010). *The physics of glaciers* (4th ed.). Elsevier.

Farinotti, D., Huss, M., Fürst, J. J., Landmann, J., Machguth, H., Maussion, F., & Pandit, A. (2019). A consensus estimate for the ice thickness distribution of all glaciers on Earth. *Nature Geoscience*, *12*(3), 168–173. https://doi.org/10.1038/s41561-019-0300-3

Gao, H., Feng, Z., Zhang, T., Wang, Y., He, X., Li, H., et al. (2021). Assessing glacier retreat and its impact on water resources in a headwater of Yangtze River based on CMIP6 projections. *Science of the Total Environment*, *765*, 142774. https://doi.org/10.1016/j.scitotenv.2020.142774

Gardner, A., Fahnestock, M., & Scambos, T. (2019). MEaSUREs ITS_LIVE regional glacier and ice sheet surface velocities [Dataset]. *NASA*. https://doi.org/10.5067/6II6VW8LLWJ7

Gilbert, A., Leinss, S., Kargel, J., Kääb, A., Gascoin, S., Leonard, G., et al. (2018). Mechanisms leading to the 2016 giant twin glacier collapses, Aru Range, Tibet. *The Cryosphere*, *12*(9), 2883–2900. https://doi.org/10.5194/tc-12-2883-2018

Gilbert, A., Sinisalo, A., Gurung, T. R., Fujita, K., Maharjan, S. B., Sherpa, T. C., & Fukuda, T. (2020). The influence of water percolation through crevasses on the thermal regime of a Himalayan mountain glacier. *The Cryosphere*, *14*(4), 1273–1288. https://doi.org/10.5194/tc-14-1273-2020

Gilbert, A., Vincent, C., Six, D., Wagnon, P., Piard, L., & Ginot, P. (2014). Modeling near-surface firn temperature in a cold accumulation zone (Col du Dôme, French Alps): From a physical to a semi-parameterized approach. *The Cryosphere*, *8*(2), 689–703. https://doi.org/10.5194/tc-8-689-2014

Han, P., Long, D., Zhao, F., & Slater, L. J. (2023). Response of two glaciers in different climate settings of the Tibetan plateau to climate change through year 2100 using a hybrid modelling approach. *Water Resources Research*, *59*(4), e2022WR033618. https://doi.org/10.1029/2022wr033618

Hock, R., Bliss, A., Marzeion, B., Giesen, R. H., Hirabayashi, Y., Huss, M., et al. (2019). Glaciermip–A model intercomparison of global-scale glacier mass-balance models and projections. *Journal of Glaciology*, *65*(251), 453–467. https://doi.org/10.1017/jog.2019.22

Hoffman, M. J., Perego, M., Price, S. F., Lipscomb, W. H., Zhang, T., Jacobsen, D., et al. (2018). MPAS-Albany Land ice (MALI): A variable-resolution ice sheet model for Earth system modeling using Voronoi grids. *Geoscientific Model Development*, *11*(9), 3747–3780. https://doi.org/10.5194/gmd-11-3747-2018

Hugonnet, R., McNabb, R., Berthier, E., Menounos, B., Nuth, C., Girod, L., et al. (2021). Accelerated global glacier mass loss in the early twenty-first century. *Nature*, *592*(7856), 726–731. https://doi.org/10.1038/s41586-021-03436-z

Huss, M. (2011). Present and future contribution of glacier storage change to runoff from macroscale drainage basins in Europe. *Water Resources Research*, *47*(7), W07511. https://doi.org/10.1029/2010WR010299

Huss, M., & Hock, R. (2018). Global-scale hydrological response to future glacier mass loss. *Nature Climate Change*, *8*(2), 135–140. https://doi.org/10.1038/s41558-017-0049-x

Immerzeel, W. W., van Beek, L. P. H., & Bierkens, M. F. P. (2010). Climate change will affect the Asian water towers. *Science*, *328*(5984), 1382–1385. https://doi.org/10.1126/science.1183188

Jay-Allemand, M., Gillet-Chaulet, F., Gagliardini, O., & Nodet, M. (2011). Investigating changes in basal conditions of Variegated Glacier prior to and during its 1982–1983 surge. *The Cryosphere*, *5*(3), 659–672. https://doi.org/10.5194/tc-5-659-2011

Kang, S., Zhang, Q., Zhang, Y., Guo, W., Ji, Z., Shen, M., et al. (2022). Warming and thawing in the Mt. Everest region: A review of climate and environmental changes. *Earth-Science Reviews*, *225*, 103911. https://doi.org/10.1016/j.earscirev.2021.103911

Khadka, M., Kayastha, R. B., & Kayastha, R. (2020). Future projection of cryospheric and hydrologic regimes in Koshi River basin, Central Himalaya, using coupled glacier dynamics and glacio-hydrological models. *Journal of Glaciology*, *66*(259), 831–845. https://doi.org/10.1017/jog.2020.51

King, O., Bhattacharya, A., Ghuffar, S., Tait, A., Guilford, S., Elmore, A. C., & Bolch, T. (2020). Six decades of glacier mass changes around Mt. Everest are revealed by historical and contemporary images. *One Earth*, *3*(5), 608–620. https://doi.org/10.1016/j.oneear.2020.10.019

Kraaijenbrink, P. D. A., Bierkens, M. F. P., Lutz, A. F., & Immerzeel, W. W. (2017). Impact of a global temperature rise of 1.5 degrees Celsius on Asia's glaciers. *Nature*, *549*(7671), 257–260. https://doi.org/10.1038/nature23878

Langhammer, L., Grab, M., Bauder, A., & Maurer, H. (2019). Glacier thickness estimations of alpine glaciers using data and modeling constraints. *The Cryosphere*, *13*(8), 2189–2202. https://doi.org/10.5194/tc-13-2189-2019

Leng, W., Ju, L., Gunzburger, M., Price, S., & Ringler, T. (2012). A parallel high-order accurate finite element nonlinear Stokes ice sheet model and benchmark experiments. *Journal of Geophysical Research*, *117*(F1), F01001. https://doi.org/10.1029/2011JF001962

Liu, Y., Hou, S., Wang, Y., & Song, L. (2009). Distribution of borehole temperature at four high-altitude alpine glaciers in Central Asia. *Journal of Mountain Science*, *6*(3), 221–227. https://doi.org/10.1007/s11629-009-0254-9

Miles, K. E., Hubbard, B., Quincey, D. J., Miles, E. S., Sherpa, T. C., Rowan, A. V., & Doyle, S. H. (2018). Polythermal structure of a Himalayan debris-covered glacier revealed by borehole thermometry. *Scientific Reports*, *8*(1), 16825. https://doi.org/10.1038/s41598-018-34327-5

Millan, R., Mouginot, J., Rabatel, A., & Morlighem, M. (2022). Ice velocity and thickness of the world's glaciers. *Nature Geoscience*, *15*(2), 124–129. https://doi.org/10.1038/s41561-021-00885-z

Perego, M., Gunzburger, M., & Burkardt, J. (2012). Parallel finite-element implementation for higher-order ice-sheet models. *Journal of Glaciology*, *58*(207), 76–88. https://doi.org/10.3189/2012JoG11J063

Radić, V., & Hock, R. (2014). Glaciers in the Earth's hydrological cycle: Assessments of glacier mass and runoff changes on global and regional scales. *Surveys in Geophysics*, *35*(3), 813–837. https://doi.org/10.1007/s10712-013-9262-y

Rounce, D. R., Hock, R., & Shean, D. E. (2020). Glacier mass change in High Mountain Asia through 2100 using the open-source python glacier evolution model (PyGEM). *Frontiers in Earth Science*, *7*, 331. https://doi.org/10.3389/feart.2019.00331

Seddik, H., Greve, R., Sakakibara, D., Tsutaki, S., Minowa, M., & Sugiyama, S. (2019). Response of the flow dynamics of Bowdoin Glacier, northwestern Greenland, to basal lubrication and tidal forcing. *Journal of Glaciology*, *65*(250), 225–238. https://doi.org/10.1017/jog.2018.106

Seroussi, H., Nowicki, S., Simon, E., Abe-Ouchi, A., Albrecht, T., Brondex, J., et al. (2019). initMIP-Antarctica: An ice sheet model initialization experiment of ISMIP6. *The Cryosphere*, *13*(5), 1441–1471. https://doi.org/10.5194/tc-13-1441-2019

Shea, J. M., Immerzeel, W. W., Wagnon, P., Vincent, C., & Bajracharya, S. (2015). Modelling glacier change in the Everest region, Nepal Himalaya. *The Cryosphere*, *9*(3), 1105–1128. https://doi.org/10.5194/tc-9-1105-2015

Tadono, T., Ishida, H., Oda, F., Naito, S., Minakawa, K., & Iwamoto, H. (2014). Precise global DEM generation by ALOS PRISM [Dataset]. *ISPRS Annals of the Photogrammetry, Remote Sensing and Spatial Information Sciences*, *2*, 71–76. https://doi.org/10.5194/isprsannals-II-4-71-2014

Thakuri, S., Salerno, F., Smiraglia, C., Bolch, T., D'Agata, C., Viviano, G., & Tartari, G. (2014). Tracing glacier changes since the 1960s on the south slope of Mt. Everest (central Southern Himalaya) using optical satellite imagery. *The Cryosphere*, *8*(4), 1297–1315. https://doi.org/10.5194/tc-8-1297-2014

Wang, Y., Zhang, T., Ren, J., Qin, X., Liu, Y., Sun, W., et al. (2018). An investigation of the thermomechanical features of Laohugou Glacier No. 12 on Qilian Shan, western China, using a two-dimensional first-order flow-band ice flow model. *The Cryosphere*, *12*(3), 851–866. https://doi.org/10.5194/tc-12-851-2018

Yan, Z., Leng, W., Wang, Y., Xiao, C., & Zhang, T. (2022). A comparison between three-dimensional, transient, thermomechanically coupled first-order and Stokes ice flow models. *Journal of Glaciology*, *69*(275), 1–12. https://doi.org/10.1017/jog.2022.77

Yao, T., Bolch, T., Chen, D., Gao, J., Immerzeel, W., Piao, S., et al., others (2022). The imbalance of the Asian water tower. *Nature Reviews Earth & Environment*, *3*(10), 618–632. https://doi.org/10.1038/s43017-022-00299-4

Zhang, T., Price, S., Ju, L., Leng, W., Brondex, J., Durand, G., & Gagliardini, O. (2017). A comparison of two Stokes ice sheet models applied to the Marine ice Sheet Model Intercomparison Project for plan view models (MISMIP3d). *The Cryosphere*, *11*(1), 179–190. https://doi.org/10.5194/tc-11-179-2017

Zhang, T., Wang, Y., & Leng, W. (2024). Projections of East Rongbuk Glacier, Mt. Everest [Dataset]. *Zenodo*, https://doi.org/10.5281/zenodo.10826389

Zhang, T., Xiao, C., Colgan, W., Qin, X., Du, W., Sun, W., et al. (2013). Observed and modelled ice temperature and velocity along the main flowline of East Rongbuk Glacier, Qomolangma (Mount Everest), Himalaya. *Journal of Glaciology*, *59*(215), 438–448. https://doi.org/10.3189/2013JoG12J202

Zhao, H., Su, B., Lei, H., Zhang, T., & Xiao, C. (2023). A new projection for glacier mass and runoff changes over High Mountain Asia. *Science Bulletin*, *68*(1), 43–47. https://doi.org/10.1016/j.scib.2022.12.004

Zhao, L., Tian, L., Zwinger, T., Ding, R., Zong, J., Ye, Q., & Moore, J. C. (2014). Numerical simulations of Gurenhekou glacier on the Tibetan Plateau. *Journal of Glaciology*, *60*(219), 71–82. https://doi.org/10.3189/2014JoG13J126

Zhao, W., Zhao, L., Tian, L., Wolovick, M., & Moore, J. C. (2022). Simulating the evolution of Da Anglong Glacier, western Tibetan Plateau over the 21st century. *Water*, *14*(2), 271. https://doi.org/10.3390/w14020271